Generation of photonic orbital angular momentum superposition states using vortex beam emitters with superimposed gratings

Qingsheng Xiao,[1,2] Charalambos Klitis,[3] Shimao Li,[1] Yueyang Chen,[1] Xinlun Cai,[1,*] Marc Sorel,[3] and Siyuan Yu[1,4]

[1]*State Key Laboratory of Optoelectronic Materials and Technologies and School of Physics and Engineering, Sun Yat-sen University, Guangzhou 510275, China*
[2]*School of Information Engineering, Jiangxi University of Science and Technology, Ganzhou, Jiangxi, 341000, China*
[3]*School of Engineering, University of Glasgow, Rankine Building, Oakfield Avenue, Glasgow G12 8LT, UK*
[4]*Department of Electrical and Electronic Engineering, University of Bristol, University Walk, Bristol, BS8 1TR, UK*
[*]*caixlun5@mail.sysu.edu.cn*

Abstract: An integrated approach to produce photonic orbital angular momentum (OAM) superposition states with arbitrary OAM spectrum has been demonstrated. Superposition states between two vector OAM modes have been achieved by integrating a superimposed angular grating in one silicon micro-ring resonator, with each mode having near equal weight. The topological charge difference between the two compositional OAM modes is determined by the difference between the numbers of elements in the two original gratings being superimposed, while the absolute values of the topological charge can be changed synchronously by switching WGM resonant wavelengths. This novel approach provides a scalable and flexible source for the OAM-based quantum information and optical manipulation applications.

OCIS codes: (050.4865) Optical vortices; (050.2770) Gratings; (130.3120) Integrated optics devices.

References and links

1. L. Allen, M. W. Beijersbergen, R. J. C. Spreeuw, and J. P. Woerdman, "Orbital angular momentum of light and the transformation of Laguerre-Gaussian laser modes," Phys. Rev. A **45**(11), 8185–8189 (1992).
2. G. Molina-Terriza, J. P. Torres, and L. Torner, "Twisted photons," Nat. Phys. **3**(5), 305–310 (2007).
3. J. Wang, J.-Y. Yang, I. M. Fazal, N. Ahmed, Y. Yan, H. Huang, Y. Ren, Y. Yue, S. Dolinar, M. Tur, and A. E. Willner, "Terabit free-space data transmission employing orbital angular momentum multiplexing," Nat. Photonics **6**(7), 488–496 (2012).
4. N. Bozinovic, Y. Yue, Y. Ren, M. Tur, P. Kristensen, H. Huang, A. E. Willner, and S. Ramachandran, "Terabit-scale orbital angular momentum mode division multiplexing in fibers," Science **340**(6140), 1545–1548 (2013).
5. N. J. Cerf, M. Bourennane, A. Karlsson, and N. Gisin, "Security of quantum key distribution using d-level systems," Phys. Rev. Lett. **88**(12), 127902 (2002).
6. D. S. Ding, W. Zhang, Z. Y. Zhou, S. Shi, G. Y. Xiang, X. S. Wang, Y. K. Jiang, B. S. Shi, and G. C. Guo, "Quantum storage of orbital angular momentum entanglement in an atomic ensemble," Phys. Rev. Lett. **114**(5), 050502 (2015).
7. G. Molina-Terriza, J. P. Torres, and L. Torner, "Management of the angular momentum of light: preparation of photons in multidimensional vector states of angular momentum," Phys. Rev. Lett. **88**(1), 013601 (2001).
8. X. Cai, J. Wang, M. J. Strain, B. Johnson-Morris, J. Zhu, M. Sorel, J. L. O'Brien, M. G. Thompson, and S. Yu, "Integrated compact optical vortex beam emitters," Science **338**(6105), 363–366 (2012).
9. M. J. Strain, X. Cai, J. Wang, J. Zhu, D. B. Phillips, L. Chen, M. Lopez-Garcia, J. L. O'Brien, M. G. Thompson, M. Sorel, and S. Yu, "Fast electrical switching of orbital angular momentum modes using ultra-compact integrated vortex emitters," Nat. Commun. **5**, 4856 (2014).
10. H. Li, M. J. Strain, L. Meriggi, L. Chen, J. Zhu, K. Cicek, J. Wang, X. Cai, M. Sorel, M. G. Thompson, and S. Yu, "Pattern manipulation via on-chip phase modulation between orbital angular momentum beams," Appl. Phys. Lett. **107**(5), 051102 (2015).
11. Y. Wang, X. Feng, D. Zhang, P. Zhao, X. Li, K. Cui, F. Liu, and Y. Huang, "Generating optical superimposed vortex beam with tunable orbital angular momentum using integrated devices," Sci. Rep. **5**, 10958 (2015).

#252927 Received 4 Nov 2015; revised 1 Jan 2016; accepted 4 Jan 2016; published 8 Feb 2016

12. N. K. Fontaine, C. R. Doerr, and L. Buhl, "Efficient multiplexing and demultiplexing of free-space orbital angular momentum using photonic integrated circuits," in Optical Fiber Communication Conference, OSA Technical Digest (Optical Society of America, 2012), OTu1I.2.
13. T. Su, R. P. Scott, S. S. Djordjevic, N. K. Fontaine, D. J. Geisler, X. Cai, and S. J. B. Yoo, "Demonstration of free space coherent optical communication using integrated silicon photonic orbital angular momentum devices," Opt. Express **20**(9), 9396–9402 (2012).
14. B. Guan, R. P. Scott, N. K. Fontaine, T. Su, C. Ferrari, M. Cappuzzo, F. Klemens, B. Keller, M. Earnshaw, and S. J. B. Yoo, "Integrated optical orbital angular momentum multiplexi ng device using 3-D waveguides and a silica PLC," in *CLEO: 2013, OSA Technical Digest (online)* (Optical Society of America, 2013), paper CTu1L.4.
15. H. Qian, B. D. Markman, and N. C. Giebink, "Vector vortex beam emission from organic semiconductor microlasers," Appl. Phys. Lett. **103**(16), 161110 (2013).
16. H. Li, D. Phillips, X. Wang, D. Ho, L. Chen, X. Zhu, J. Zhu, S. Yu, and X. Cai, "Orbital angular momentum (OAM) vertical-cavity-surface-emitting lasers," Optica **2**(17), 21 (2015).
17. M. J. Strain, S. Thoms, D. S. MacIntyre, and M. Sorel, "Multi-wavelength filters in silicon using superposition sidewall Bragg grating devices," Opt. Lett. **39**(2), 413–416 (2014).
18. S. H. Tao, X. C. Yuan, J. Lin, and R. E. Burge, "Residue orbital angular momentum in interferenced double vortex beams with unequal topological charges," Opt. Express **14**(2), 535–541 (2006).
19. V. Yu. Bazhenov, M. S. Soskin, and M. V. Vasnetsov, "Screw dislocations in light wavefronts," J. Mod. Opt. **39**(5), 985–990 (1992).
20. G. Gibson, J. Courtial, M. Padgett, M. Vasnetsov, V. Pas'ko, S. Barnett, and S. Franke-Arnold, "Free-space information transfer using light beams carrying orbital angular momentum," Opt. Express **12**(22), 5448–5456 (2004).
21. G. Gibson II, J. Courtial, M. Vasnetsov, S. Barnett, S. Franke-Arnold, and M. Padgett, "Increasing the data density of free-space optical communications using orbital angular momentum," Proc. SPIE **5550**, 367–373 (2004).
22. S. A. Schulz, T. Machula, E. Karimi, and R. W. Boyd, "Integrated multi vector vortex beam generator," Opt. Express **21**(13), 16130–16141 (2013).
23. D. Zhang, X. Feng, and Y. Huang, "Encoding and decoding of orbital angular momentum for wireless optical interconnects on chip," Opt. Express **20**(24), 26986–26995 (2012).
24. M. Padgett and R. Bowman, "Tweezers with a twist," Nat. Photonics **5**(6), 343–348 (2011).

1. Introduction

Orbital angular momentum (OAM) of photons, discovered in 1992, represents an additional intrinsic degree of freedom of a light beam or a single photon, in addition to the ones (e.g. polarization) widely exploited in current photonic technologies [1,2]. OAM is associated with the transverse spatial structure of the wave front. While polarization is characterized by two orthogonal bases, OAM is defined in an unbounded infinite-dimensional Hilbert space for photons. Therefore it is in principle possible to encode a much larger amount of information in the OAM degree of freedom than in the case of polarization, e.g. achieving greater information transmission capacity [3,4], as well as allowing for more secure communication protocols [5] and greater density of quantum information storage [6]. light beams with OAM also provides unique opportunities for manipulation of micro-/nano-particles as it asserts torque in addition to forces related to optical intensity gradient, giving rise to orbital and spin movements in addition to trapping [2,7]. This makes OAM highly attractive for applications in areas as diverse as future optical communication, quantum information, biology, chemistry and microfluidics, etc.

The practical applications of OAM have been greatly benefit from photonic integration due to its advantages in reliability, miniaturization, and scalability compared to bulk optics. Recently, a new chip-scale device [8] that enables OAM beams to be efficiently generated directly from a compact photonic integrated circuit (PIC) is demonstrated. The operation principle of the device is based on the coupling of whispering gallery modes (WGMs) in a micro-ring resonator to free-space propagating OAM modes through an angular grating embedded within the micro-resonator. By detuning the wavelength of WGM from the Bragg resonance (e.g., by changing input wavelength [8] or by detuning the ring resonance from the input wavelength using integrated electrically addressable thermal phase shifters within the resonator [9]) this device is capable of generating OAM states with single but variable topological charge. The electrical detuning also enabled on-off keying OAM modes at record rates of ~15 μs [9]. An functional PIC composed of an OAM emitter and a 3dB coupler that

#252927 Received 4 Nov 2015; revised 1 Jan 2016; accepted 4 Jan 2016; published 8 Feb 2016

can be used to generate and manipulate OAM superposition states was also reported [10], in which the input light simultaneously excited the clockwise and anticlockwise WGMs in the micro-ring resonator and thereby generated two OAM states with equal but opposite topological charge. The relative phase between the two OAM states could be actively modulated by a phase shifter integrated with the input waveguide. More recently, another similar device consisting of a variable amplitude splitter (VAS) and an OAM emitter, was proposed [11], in which the relative amplitude of the two OAM states with opposite chirality could be tuned. In addition, different from this azimuthal grating coupling mechanism, several approaches such as waveguide-array-based radial grating coupling device [12,13], hybrid 3D PIC device [14], organic semiconductor microdisk laser [15] and micro-scale Spiral Phase Plate integrated VCSEL [16] have been demonstrated readily OAM generating and (de-) multiplexing (multiple OAM states superposition) functions. These devices demonstrated the on-chip dynamical manipulation of OAM states and its potential for the development of sophisticated OAM functions on scalable and compact PICs.

Here we demonstrate another extremely simple and scalable approach to generate OAM superposition states by integrating superimposed angular gratings in a single WGM resonator. This approach could generate arbitrary superposition of OAM states with the same or opposite chirality. The topological charge difference between the OAM states is determined by the difference in the number of element in the original gratings being superimposed, while the absolute values of the topological charge can be varied by detuning the cavity resonant with respect to the light wavelength. The relative weight of the OAM states can be varied by varying the size of the grating elements.

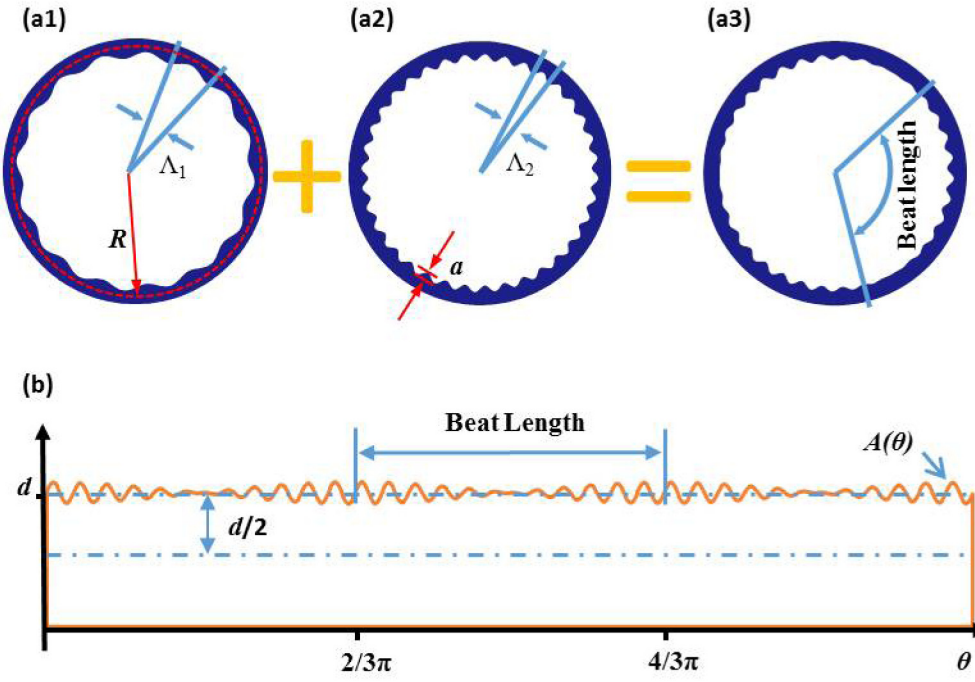

Fig. 1. Structure of the superimposed grating device. (a) Schematic of two single grating (with period of Λ_1 and Λ_2, respectively) superimposed into multiple-beat modulated device, here shows the three beats device. (b) an unfolded view of (a3).

2. Concepts and structures

Similar to [8], the operation principle of the device is based on the coupling of whispering gallery modes (WGMs) in a micro-ring resonator to free-space propagating OAM modes

#252927 Received 4 Nov 2015; revised 1 Jan 2016; accepted 4 Jan 2016; published 8 Feb 2016

through angular gratings embedded within the micro-resonator. The generated OAM mode order, *l*, is defined by the resonant WGM order, *p*, and the number of scattering elements in the ring, *q*, as $l = p - q$.

The concepts and structures of the superimposed angular grating device are illustrated in Fig. 1. To create superposition states of OAM in a similar device, superimposed gratings, similar to those used to realize multiple-filter stopbands around the target Bragg wavelengths in a single integrated Bragg grating device [17], are introduced into the WGM resonator. Here two sets of angular gratings with different periods (Λ_1 and Λ_2) have been superimposed onto a ring resonator, which generates a superimposed grating envelope with multiple beat perturbations, as shown in Fig. 1(a3). Sinusoidal shaped profiles are chosen for each grating and they are simply summed to give an effective and achievable superpositional waveguide width variation. The superimposed angular grating perturbation as a function of the azimuthal angles, θ , in the polar coordinate centered at the center of the micro-ring, $A(\theta)$, can be written as

$$A(\theta) = a_1 \sin(q_1\theta) + a_2 \sin(q_2\theta) \tag{1}$$

Where $q_1 = 2\pi R/\Lambda_1, q_2 = 2\pi R/\Lambda_2$ are the numbers of grating elements in the two single gratings, R is the radius of ring resonator. a_1 and a_2 are the amplitude of the sinusoidal gratings, which are set to the same value in this work in order to obtain equal weight for the two OAM modes. Based on the grating perturbation function above, the waveguide boundary for the inner side-wall can be expressed as $\rho(\theta) = R - d/2 + A(\theta)$ and the smooth outside wall as $\rho(\theta) = R - d/2$, respectively, where d is the average width of the ring waveguide. For the purpose of illustration, the superimposed angular gratings OAM emitter in Fig. 1(a3) was unfolded into a linear structure, as shown in Fig. 1(b). The upper boundary profile of the unfolded waveguide is defined by $A(\theta)$, which produced a beat pattern that modulates the original gratings with a number of periods given by the difference of the grating element numbers $\Delta q = q_1 - q_2$ within the azimuthal angle range of [0, 2π]. For example, as shown in Fig. 1(b), two sets of single grating with elements of $q_1 = 73$ and $q_2 = 76$ have been used to generate the three-beat superimposed grating, each beat having a length of $2\pi/3$.

The superimposed grating devices were fabricated on a conventional SOI platform with *220 nm* silicon core and *2um* buried oxide lower cladding. The width and the height of waveguides were defined as *500nm* and *220nm*, respectively. The inner radius of the ring cavity is *7.5um* and the gap between the bus waveguide and ring cavity is *100 nm*. The superimposed angular grating perturbation are located around this inner radius with an amplitude of $a_{1,2} = 20nm$.

To verify the concept, several samples with one-, two-, and three-beat superimposed gratings have been fabricated, expected to realize superimposing OAM modes with topological charge difference of $l_1 - l_2 = 1, 2, 3$ respectively. These contain three combinations of [$q_1 = 74, q_2 = 75$], [$q_1 = 74, q_2 = 76$], and [$q_1 = 73, q_2 = 76$]. All structures are patterned into hydrogen silsequioxane (HSQ) resist by means of electron-beam lithography, which is then used as a hard mask for Reactive Ion Etching (RIE) of the silicon layer. Finally, a 900nm SiO_2 upper cladding layer was coated onto the device by plasma-enhanced chemical vapor deposition (PECVD).

#252927 Received 4 Nov 2015; revised 1 Jan 2016; accepted 4 Jan 2016; published 8 Feb 2016

3. Characterization and results

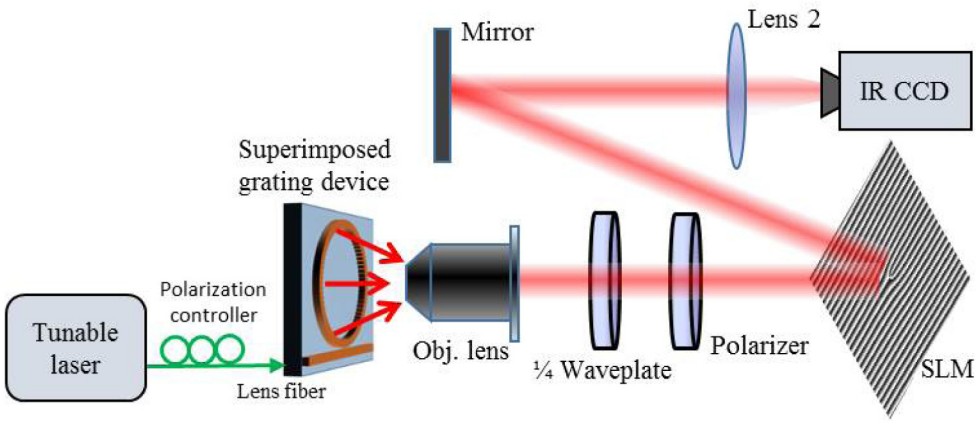

Fig. 2. The experimental setup for characterization the superposition OAM modes.

Figure 2 shows the measurement setup. The light from a tunable laser is coupled into the bus waveguide using a tapered lens fiber. A fiber-optic polarization controller (PC) is used to ensure quasi-TE mode excitation in the silicon waveguide. The polarization of the mode could be verified by monitoring the transmitted power from the other port of the bus waveguide. By scanning the wavelength of the tunable laser to coincide with the micro-ring resonances, WGMs would be excited and scattered into radiation beam by the superimposed angular gratings. A large numerical aperture objective lens is used to collimate the radiated beam. When the device is located at the front focal plane of the objective lens, the Fourier transform of the radiation field could be found in its back focal plane, which can be used for analyzing the far-field properties of the radiation. The transmission spectra (through the bus waveguide) and the radiation spectra,which play a guiding role in the measurement followed, have been obtained by collecting the output power of the access waveguide and by monitoring the full power behind the objective lens using a photo-detector respectively, while scanning the wavelength of the input laser. Moreover, we have made a measurement similar to Ref [8]. on the emission efficiency of the chip. The coupling loss is −3dB per facet, the waveguide transmission loss is 2.5dB/cm, waveguide to free space output efficiency is 10%, and the overall efficiency is around 4%.

The near-field and far-field of the radiated beams have been observed and studied. An imaging system consisting of a focusing lens and an IR-CCD camera located at its back focal plane is placed in the optical path after the objective lens to take photograph of the near-field images.

The near-field patterns of the two-beat grating device and the three-beat grating device are presented in Figs. 3(g) and 3(i), in which two or three crescent-shaped lobes are arranged in circular arrangement respectively, in very good alignment with the envelope profile of the superimposed angular grating device, indicating that the radiated beams are actually emitted from the modulated gratings.

#252927 Received 4 Nov 2015; revised 1 Jan 2016; accepted 4 Jan 2016; published 8 Feb 2016

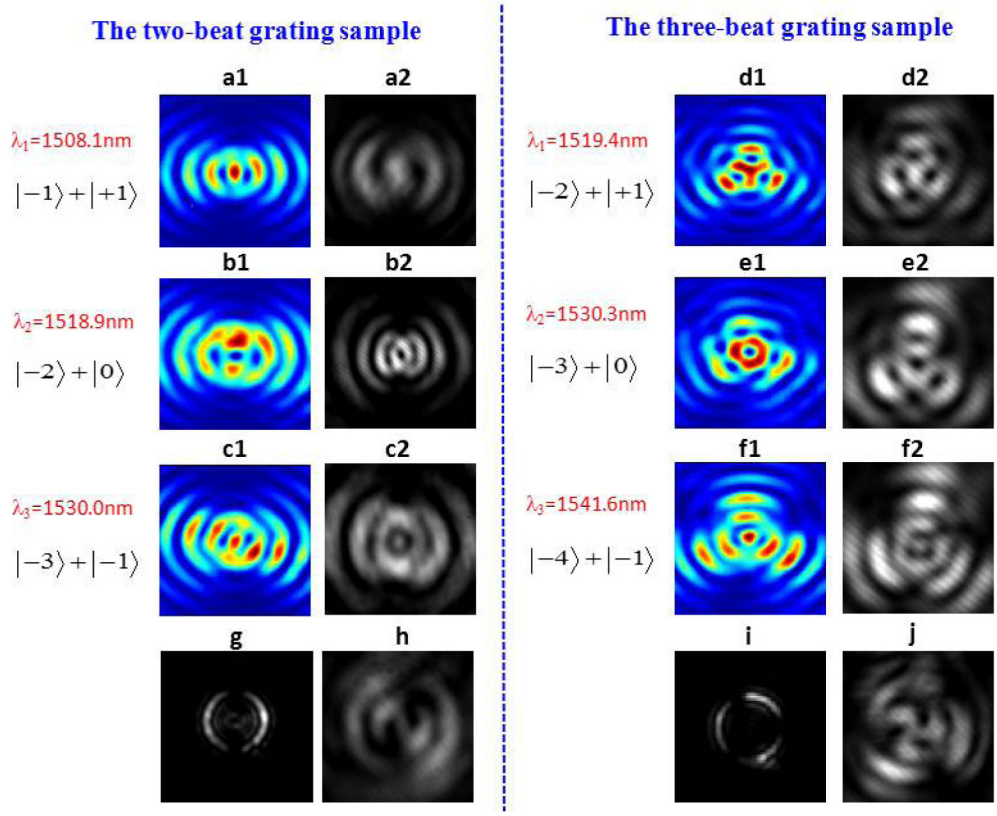

Fig. 3. The far-field patterns of the two-beat grating device (a1~c1: FDTD simulated, a2~c2: measured) and the three-beat grating device (d1~f1: FDTD simulated, d2~f2: measured). Their near-field patterns are showing in (g) and (i). And the well-defined spiral interference fringes existed at appropriate locations are showing in (h) and (j).

As shown in Fig. 3, several measured far-field images of the two-beat grating device and the three-beat grating device are listed in left column Fig. 3(a2-c2) and right column Fig. 3(d2-f2), respectively. They are measured at different resonant wavelengths according to the transmission/radiation spectrum so that different combinations of topological charge are obtained, indicated to their left. For example, the Fig. 3(a2) is a far-field of the two-beat grating sample at wavelength of 1508.1 nm. On this wavelength, the resonant WGM order of the ring-shaped device is $p = 75$, and the scattering element numbers of the two gratings being superimposed are $q_1 = 74$ and $q_2 = 76$, so this beam is carrying an OAM superposition state of $|-1\rangle+|+1\rangle$ according to $l = p - q$. When the wavelength transfers to the next resonant peak of 1518.9nm, the p transfers to 74, so another OAM superposition state of $|-2\rangle+|0\rangle$ is obtained, Fig. 3(b2). Along this approach, all combinations of topological charge could be achieved in principle. The corresponding FDTD simulation results are presented in the color images of Fig. 3(a1-c1) and Fig. 3(d1-f1). It can be seen that the measurement results agree very well with the simulations.

These complex patterns can be explained by interference of the two vector OAM modes. As the two emitted OAM modes have different topologic charges, they are not always spatially overlapping during propagation despite emitted from the same location on the ring. So there will exist residual OAM in the non-overlapping areas [18] and the residual OAM may be located on different concentric rings and may have opposite orientations, which result in the complex patterns.

#252927 Received 4 Nov 2015; revised 1 Jan 2016; accepted 4 Jan 2016; published 8 Feb 2016

Another factor contributing in the complex patterns is the vector characteristics of the radiated modes. The different state-of-polarization (SoP) evolution of the different vector OAM modes means that vector field components cannot be perfectly aligned even though they overlapped in the interference areas which give rise to complex interference fringes.

However, in the center of the patterns, well-defined spiral interference fringes have been observed at appropriate locations depending on the topological charge difference between the two superimposed OAM modes and the focus length of the objective lens, as shown in Figs. 3(h) and 3(j). It can be seen that the innermost rings or the center spots of the two modes overlap and interfere to form the spiral arms characteristic of the OAM modes [8,19]. The number of the spiral arms is equal to the topological charge difference between the two superimposed OAM modes.

To confirm the OAM components, a spatial light modulator (SLM) based OAM analysis system have been used, as shown in Fig. 2. The SLM used in our experiment is HOLOEYE PLUTO 1550, which is located behind the objective lens. As the SLM can only respond correctly to a fixed linear polarization, a polarization filter which consists of a 1/4 wave-plate and a polarizer have been inserted in front of the SLM to select the matching polarization for the SLM. Either the left hand circularly polarized (LHCP) or the right hand circularly polarized (RHCP) component of the radiation beam is converted into a linearly polarized beam with an OAM value *l-1* or *l + 1*, depending on the relative angle between the axis of the quarter-wave plate and the polarizer, as our previous work demonstrated [8,9]. As the LHCP or RHCP component are from the same emitted mode and don't affect the results in this work, we choose the RHCP. The linearly polarized beam is projected onto the SLM and diffracted by fork grating holograms [20] controlled by a computer. The diffracted beam is focused or Fourier transformed by Lens 2 and then projected on an IR-CCD camera. By changing the fold value, *H*, of the fork dislocation in the grating holograms, the OAM mode components in the linearly polarized beam will be in turn transformed into the 0th-order mode (Gaussian beam) with a bright center. By reading the on-axis intensity of each image captured on the IR-CCD camera, the relative weight of the corresponding OAM mode components could be measured [9,20].

Using this system, the radiation beams from the two-beat grating device and from the three-beat grating device have been measured as shown in first row and second row of Fig. 4, respectively. A central bright spot can be observed in two images in both row (marked with red frames), indicating that there are two OAM modes matching the fork gratings displaying on the SLM. The corresponding fold values *H* of the fork gratings identify the topological charge of the two superimposed OAM modes. For example, Figs. 4 (a2) and 4(a4) in the first row correspond to fork gratings with fold values of $H = -2$ and $H = 0$, indicating that the RHCP beam consists of two OAM modes with topological charges of *-2* and *0* when we select the *-1st-order* diffracted beam for studying [21]. Therefore the original radiated beam consists of two vector OAM modes with topological charge of ± 1.

The OAM spectrum of the superposition OAM states can be measured by recording the on-axis intensity of a series of SLM-diffracted patterns while changing *H*. As shown in Figs. 4 (c) and 4(d), where histograms corresponding to row *a* and *b* are plotted. The insets are the corresponding far-field patterns of the superposition OAM states being analyzed. The normalized weight of the two radiated beams are nearly equally distributed into states $|-1\rangle$ and $|+1\rangle$ with the values of 45% and 41% (Fig. 4(c)), and into states $|-1\rangle$ and $|+2\rangle$ with the values of 36% and 34% (Fig. 4(d)), respectively. The total weight of the two main superimposed states exceeds 80%. The mode purity degradation may be attributed to the misalignment of the optics in the measurement setup.

#252927 Received 4 Nov 2015; revised 1 Jan 2016; accepted 4 Jan 2016; published 8 Feb 2016

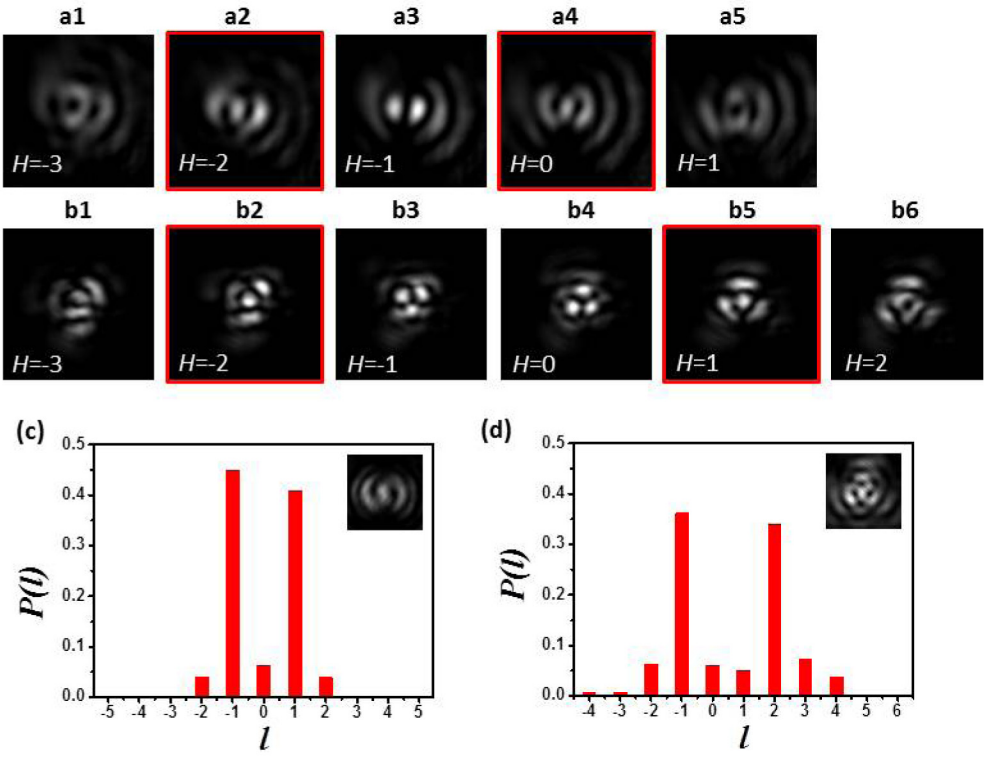

Fig. 4. The SLM diffracted patterns of a beam (inset of (c)) emitted from the two-beat grating device (a1~a5) and a beam (inset of (d)) emitted from the three-beat grating device (b1~b6). The corresponding mode spectrum are displayed in (c) and (d).

4. Conclusion and discussion

We have demonstrated an integrated device capable of emitting beams carrying superposition photonic OAM states, by means of superimposed angular gratings embedded into WGM micro-ring resonators. The topological charge difference between the individual OAM states in the superposition state is determined by the beat number between the superimposed gratings, while the absolute values of their topological charge can be changed synchronously when switching the resonant wavelengths. With two gratings of the same amplitude, the relative weight of the two states has been shown to be nearly equal. In accordance with this approach, the superposition of more OAM modes, can be realized conveniently by superimposing more sets [17] of gratings onto the micro-ring device, with the composition of the OAM spectrum being determined by the individual gratings used. It should be noted that the number of the superimposed OAM states will be limited by the fabrication resolution of electron beam lithography, although in theory there is no upper limit.

Compared to the previous works [10,11], the integrated device demonstrated in this manuscript is more compact as it does not require the assistance of other integrated components, like 3dB couplers or MZIs. Moreover, the current device have the potential of generating superposition states of more than 2 dimensions by simply putting more gratings, while the previous devices can only generate 2 dimensional superposition states. For purposes that do not require the *multiplexing* of different light beams into different OAM modes, this scheme is far simpler than what was proposed in [22], and also maintains very stable phase between the OAM states as all modes are emitted from the same source mode via the same superimposed grating. It opens up a wide range of opportunities and possibilities for applications in quantum information and optical manipulations. For example, by increasing

#252927 Received 4 Nov 2015; revised 1 Jan 2016; accepted 4 Jan 2016; published 8 Feb 2016

the number of composition OAM modes in the superposition, it is possible to provide arbitrary OAM *qudit* states for quantum encoding and quantum key distribution (QKD) applications [22,23]. In addition, the complex light field created by interfering double or multi-OAM beams with unequal topological charges, which have been shown to be useful in measurement of an object's torque by fixing the object's outer part and rotating the inner part [18], could be used to trap and drive particles in varieties of manners. As it is easy to integrate this compact device into microfluidic experimental platforms for particle manipulation, the superimposed vortex beam carrying different topological charges based on this approach could find their applications in the microfluidic area [24].

Acknowledgments

The authors wish to thank the staff of the James Watt Nanofabrication Centre at the University of Glasgow. This work was partially supported by the National Basic Research Program of China (project No. 2014CB340000), the National Natural Science Foundation of China (NSFC) (Project No. 61490715 and No.11365011), and the EPSRC under the Cornerstone project (EP/L021129/1) and the H2020-ICT-2014-1 ROAM project (645361). Xinlun Cai acknowledges the support of the "Young 1000-Talent Plan" by the Government of China.

#252927 Received 4 Nov 2015; revised 1 Jan 2016; accepted 4 Jan 2016; published 8 Feb 2016